

## Experimental study of parametric dependence of electron-scale turbulence in a spherical tokamak<sup>a)</sup>

Y. Ren,<sup>1,b)</sup> W. Guttenfelder,<sup>1</sup> S. M. Kaye,<sup>1</sup> E. Mazzucato,<sup>1</sup> R. E. Bell,<sup>1</sup> A. Diallo,<sup>1</sup> C. W. Domier,<sup>2</sup> B. P. LeBlanc,<sup>1</sup> K. C. Lee,<sup>2</sup> D. R. Smith,<sup>3</sup> and H. Yuh<sup>4</sup>

<sup>1</sup>Princeton Plasma Physics Laboratory, Princeton, New Jersey 08543, USA

<sup>2</sup>University of California at Davis, Davis, California 95616, USA

<sup>3</sup>University of Wisconsin-Madison, Madison, Wisconsin 53706, USA

<sup>4</sup>Nova Photonics, Inc., Princeton, New Jersey 08540, USA

(Received 10 February 2012; accepted 4 May 2012; published online 31 May 2012)

Electron-scale turbulence is predicted to drive anomalous electron thermal transport. However, experimental study of its relation with transport is still in its early stage. On the National Spherical Tokamak Experiment (NSTX), electron-scale density fluctuations are studied with a novel tangential microwave scattering system with high radial resolution of  $\pm 2$  cm. Here, we report a study of parametric dependence of electron-scale turbulence in NSTX H-mode plasmas. The dependence on density gradient is studied through the observation of a large density gradient variation in the core induced by an edge localized mode (ELM) event, where we found the first clear experimental evidence of density gradient stabilization of electron-gyro scale turbulence in a fusion plasma. This observation, coupled with linear gyro-kinetic calculations, leads to the identification of the observed instability as toroidal electron temperature gradient (ETG) modes. It is observed that longer wavelength ETG modes,  $k_{\perp} \rho_s \lesssim 10$  ( $\rho_s$  is the ion gyroradius at electron temperature and  $k_{\perp}$  is the wavenumber perpendicular to local equilibrium magnetic field), are most stabilized by density gradient, and the stabilization is accompanied by about a factor of two decrease in electron thermal diffusivity. Comparisons with nonlinear ETG gyrokinetic simulations show ETG turbulence may be able to explain the experimental electron heat flux observed before the ELM event. The collisionality dependence of electron-scale turbulence is also studied by systematically varying plasma current and toroidal field, so that electron gyroradius ( $\rho_e$ ), electron beta ( $\beta_e$ ), and safety factor ( $q_{95}$ ) are kept approximately constant. More than a factor of two change in electron collisionality,  $\nu_e^*$ , was achieved, and we found that the spectral power of electron-scale turbulence appears to increase as  $\nu_e^*$  is decreased in this collisionality scan. However, both linear and nonlinear simulations show no or weak dependence with the electron-ion collision frequency,  $\nu^{e/i}$ . Instead, other equilibrium parameters (safety factor, electron density gradient, for example) affect ETG linear growth rate and electron thermal transport more than  $\nu^{e/i}$  does. Furthermore, electron heat flux predicted by the simulations is found to have an order-of-magnitude spatial variation in the experimental measurement region and is also found to be much smaller than experimental levels except at one radial location we evaluated. The predicted electron heat flux is shown to be strongly anti-correlated with density gradient, which varies for a factor of three in the measurement region, which is in agreement with the density gradient dependence study reported in this paper. © 2012 American Institute of Physics. [<http://dx.doi.org/10.1063/1.4719689>]

### I. INTRODUCTION

Microturbulence is considered to be a major candidate in driving anomalous transport in fusion plasmas.<sup>1</sup> Understanding and thus controlling microinstabilities remain one of the most challenging problems in the controlled magnetic fusion research. The long-wavelength (ion-scale) ion temperature gradient (ITG) mode,<sup>2</sup> trapped electron mode (TEM),<sup>3</sup> micro-tearing mode,<sup>4-6</sup> and the short-wavelength (electron-scale) electron temperature gradient (ETG) mode<sup>7</sup> are well-known instabilities, which could drive microturbulence in fusion plasmas. In particular, although the theoretical analysis of ETG dates back to late 1970s, its effectiveness in

driving anomalous electron thermal transport has only been recognized quite recently as in Ref. 8 where the formation of radially elongated turbulence eddies (radial streamers) was identified as the reason for enhanced transport. The formation of streamers was found to be facilitated by its weaker zonal flow damping and secondary instabilities than ITG/TEM turbulence.<sup>8</sup> Furthermore, ETG is also less susceptible to  $E \times B$  flow shear than for ITG/TEM, since its linear growth rate is usually much higher than  $E \times B$  shearing rate except when it is marginally unstable.<sup>9</sup>

The National Spherical Tokamak Experiment (NSTX) has been proven as a valuable laboratory for studying electron-scale turbulence and its relation to plasma transport. Its near Mach flow, yielding large values of the  $E \times B$  shear rates, and low aspect ratio are believed to be important for the suppression of long wavelength microturbulence and the

<sup>a)</sup>Paper T12 2, Bull. Am. Phys. Soc. **56**, 278 (2011).

<sup>b)</sup>Invited speaker.

associated transport.<sup>10</sup> In typical H-mode plasmas, the ion thermal transport is found to be at the neoclassical level,<sup>11</sup> and, in most operating regimes, the dominant thermal loss is through the electron channel. In addition, the low toroidal field leads to a large electron gyroradius, which facilitates measuring turbulence wavenumber spectrum. Indeed, in a previous study, an electromagnetic ETG transport model has been applied to an NSTX RF-heated L mode plasma and good agreement with measurements have been found,<sup>12</sup> although there was no measurement of electron-scale turbulence. In order to make direct measurements, a novel 280 GHz microwave scattering system (the high- $k$  scattering system) was implemented on NSTX,<sup>13</sup> and this diagnostic has provided first experimental evidence of ETG turbulence in NSTX RF-heated L mode plasmas.<sup>14</sup> It was found that measured electron-scale turbulence is driven by the electron temperature gradient, and the observed critical gradient for linear instability is shown to be consistent with linear gyrokinetic calculations for the ETG mode. Further investigations have shown that the observed mode frequency and linear growth rate are in agreement with linear gyrokinetic calculations,<sup>15</sup> and suppression of electron-scale turbulence by  $E \times B$  flow shear was observed in NSTX neutral beam injection (NBI)-heated H-mode plasmas<sup>9</sup> consistent with turbulence theory. However, we note that the experimental study of the relation of electron-scale turbulence to plasma transport is still in its early stage, and only recently has a correlation between ETG turbulence and plasma transport been reported.<sup>15–18</sup> In Refs. 15 and 18, suppression of electron-scale turbulence by reversed magnetic shear in formation of electron internal transport barrier (eITB) is demonstrated, and the suppression is shown to be consistent with ETG physics. A recent breakthrough in the study of electron-scale turbulence on NSTX is the observation of density gradient stabilization of electron-gyro scale turbulence in a NBI-heated H-mode plasma and the accompanied factor of 2 decrease in the plasma effective thermal diffusivity.<sup>17</sup>

In this paper, we not only present a more detailed study of the density gradient stabilization of electron-scale turbulence but also extend our research beyond Ref. 17 to investigate the collisionality dependence, which is motivated by the observation of the unique spherical tokamak confinement scaling,  $B_T \tau_E \sim 1/\nu_e^*$ ,<sup>11</sup> where  $B_T$  is the toroidal field,  $\tau_E$  is the energy confinement time, and  $\nu_e^*$  is the electron collisionality. In the studies reported here, electron-scale turbulence is measured by the high- $k$  scattering system used in previous studies,<sup>13</sup> but with improved stability and scattering schemes. The former is due to the installation of a solid-state microwave source and the latter allows simultaneous measurement of more wavenumbers than previously reported. We found that a large increase in core density gradient [induced by an event of edge localized mode (ELM)] can significantly decrease turbulence spectral power for longer wavelength ETG modes,  $k_\perp \rho_s \lesssim 10$ . This observation is found to be in quantitative agreement with linear numerical simulations and supports the conclusion that the observed density fluctuations are driven by ETG modes. Furthermore, we show that the electron thermal diffusivity is decreased by about a factor of two as electron-scale turbulence is reduced by the

ELM-induced large density gradient. Corresponding nonlinear ETG gyrokinetic simulations have been carried out with GYRO code,<sup>19,20</sup> where good agreement with experiment in electron heat flux is found before the ELM event, but not after the ELM event due to the stabilization from increased density gradient. We also studied the electron collisionality dependence of electron-scale turbulence by varying plasma current ( $I_p$ ) and toroidal field ( $B_T$ ) with  $I_p/B_T$  kept constant, so we were able to keep  $\rho_e$ ,  $\beta_e$ , and  $q_{95}$  approximately constant. More than factor of two change in electron collisionality,  $\nu_e^*$ , was successfully achieved. It is found that the spectral power of electron-scale turbulence increases as  $\nu_e^*$  is decreased during the experimental scan. However, linear stability analysis using the GS2 code<sup>21</sup> shows that the linear ETG growth rates shown no dependence on the electron-ion collision frequency,  $\nu^{e/i}$ . Instead, small variations in other equilibrium parameters, e.g., safety factor ( $q$ ) and electron density gradient ( $a/L_{ne}$ ), affect ETG linear growth rate much more than  $\nu^{e/i}$  does. Nonlinear ETG gyrokinetic simulations using GYRO confirmed the weak dependence on collisionality observed in linear analysis. Furthermore, electron heat flux predicted by the nonlinear gyrokinetic simulations is found to have an order-of-magnitude spatial variation in the experimental measurement region and is also found to be much smaller than experimental levels except at one radial location we evaluated. We emphasize that the predicted electron heat flux is strongly anti-correlated with density gradient which varies a factor of three in the measurement region, demonstrating the importance of the density profile in controlling ETG-induced electron thermal transport.

The organization of this paper is as follows. We present details of the experimental setup in Sec. II. The effect of density gradient stabilization on electron scale turbulence is presented in Sec. III. The study on electron collisionality dependence is presented in Sec. IV. We will discuss and summarize our results in Sec. V.

## II. EXPERIMENTAL APPARATUS

Figure 1 plots the scattering configuration of the high- $k$  scattering system<sup>13</sup> used in the density gradient dependence study, including the probe beam and scattered beam trajectories calculated using a ray tracing code. The five receiving channels cover a wavenumber range of  $5 \text{ cm}^{-1} \lesssim k_\perp \lesssim 30 \text{ cm}^{-1}$  with a resolution of about  $1 \text{ cm}^{-1}$ , and five heterodyne receivers allow us to distinguish the wave propagation direction for each different wavenumber. Heterodyne detection is carried out in two mixing stages. The first stage down converts frequency from 280 GHz to 880 MHz by mixing scattered light and a reference signal split from the probe beam with a 279.2 GHz local oscillator signal generated by a Gunn oscillator. The second stage uses inphase-quadrature(I/Q) demodulators to mix the down-converted 880 MHz scattered signals with the reference signal to generate inphase and quadrature signals, from which we determine the phase and amplitude of the scattered wave. The power response of each receiving channel was calibrated with a solid-state microwave source with known output power. The frequency response of the scattering system is about 5 MHz. A radial resolution of  $\Delta R \approx \pm 2 \text{ cm}$ , determined by the  $1/e$  half width of the

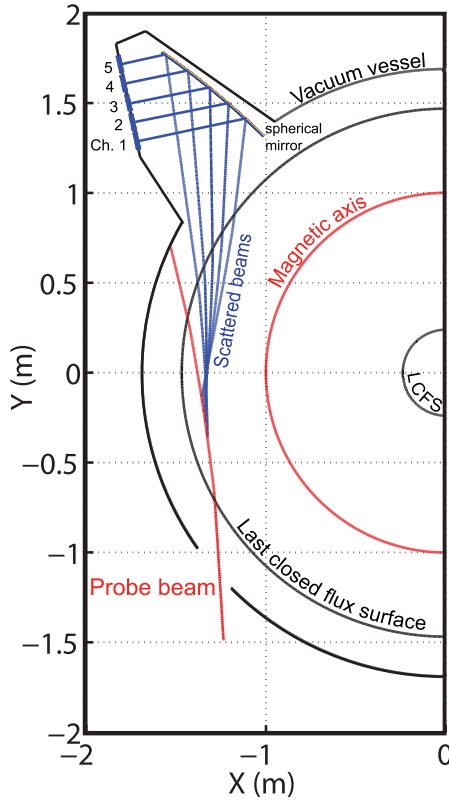


FIG. 1. Schematic of a scattering configuration of the high- $k$  scattering system on NSTX. The probe beam and scattered beam trajectories are calculated using a ray-tracing code. Scattered light is reflected and focused by a spherical mirror onto five collection windows.

microwave beam power, is the unique feature of the scattering system. This is made possible by the tangential launching scheme along with the large toroidal curvature of NSTX due to its low aspect ratio, which leads to a scattering volume much smaller than that from the overlapping of the probe and scattering beams.<sup>22</sup> This fine radial resolution allowed us to study the dependence of locally measured turbulence on local equilibrium quantities, e.g.,  $L_{T_e}$ ,<sup>14</sup>  $L_{n_e}$ ,<sup>17</sup>  $q$  (safety factor), and  $\hat{s}$  (magnetic shear).<sup>15</sup> We note that several improvements to the scattering system have significantly improved its stability and data quality. The 280 GHz probe beam is generated by a solid-state microwave source with an output power up to about 34 mW, and this source is much more stable than the back wave oscillator used previously. The scattering scheme has also been improved to significantly reduce stray radiation, which made it possible to obtain scattering signals from all five channels simultaneously, compared to at most three channels previously. Newly implemented remote control capability allows between-shot adjustment of launching and receiving optics, which made it possible to optimize scattering configuration according to realized plasma equilibria. We note that due to the tangential launching scheme employed (see Fig. 1), the scattering system measures mostly radial wavenumber,  $k_r$ , and finite but smaller poloidal wavenumber,  $k_\theta$ , e.g., a range of  $k_r \rho_s \sim 6 - 20$  and a range of  $k_\theta \rho_s \sim 2 - 4$  for the experiments presented in this paper. We would also like to emphasize that although the diagnostic does not measure the theoretically predicted most unstable modes or modes with

the largest power (modes with finite  $k_\theta$  and  $k_r \sim 0$ ), the change in  $k_r$  spectra observed in experiment still represents overall change in turbulence strength as we have observed in nonlinear ETG simulations.

### III. STUDY OF DENSITY GRADIENT DEPENDENCE

In the literature, density gradient has been predicted to stabilize ITG and ETG, but to stabilize or destabilize TEM depending on collisionality.<sup>23</sup> The stability of these micro-instabilities can often be quantified by some critical gradient depending on the source of free energy. In particular, ITG and ETG stability are described by the critical temperature gradient at which an instability is marginally unstable. For example, in Ref. 24, an analytic form of the critical temperature gradient for ETG instability is determined from many linear gyrokinetic simulations

$$(R_0/L_{T_e})_{crit} = \max \left\{ \left( 1 + Z_{eff} \frac{T_e}{T_i} \right) (1.33 + 1.99\hat{s}/q)(\dots), \right. \\ \left. 0.8R_0/L_{n_e} \right\}, \quad (1)$$

where  $R_0$  is the major radius of the flux surface center,  $L_{T_e} = (d \ln T_e / dr)^{-1}$  is the electron temperature scale length,  $L_{n_e} = (d \ln n_e / dr)^{-1}$  is the electron density scale length,  $Z_{eff}$  is the effective ionic charge,  $T_e$  is the electron temperature,  $T_i$  is the ion temperature, and  $(\dots)$  denotes some geometric terms not easily quantifiable for low aspect ratio tokamaks. We would like to emphasize that Eq. (1) explicitly shows that if density gradient is large enough, the second term in the  $\max$  function,  $0.8R_0/L_{n_e}$ , can overcome the first term and result in determining the critical temperature gradient by density gradient alone. Thus, large density gradient may stabilize ETG instability and lead to improvement in energy confinement. Indeed, confinement improvements have been observed to be associated with peaked density profile resulting from pellet injection,<sup>25</sup> and the improvements were attributed to density gradient, perpendicular flow shearing, and/or reversed magnetic shear.<sup>26-28</sup> However, first direct experimental demonstration of density gradient stabilization of plasma turbulence was only reported more recently in Ref. 17, where a large density gradient increase was induced in the core by an ELM,<sup>29</sup> and longer wavelength electron-scale modes,  $k_\perp \rho_s \lesssim 10$ , are found to be strongly stabilized. Here, we present a more detailed study of the experimental observations together with linear and nonlinear gyrokinetic simulations.

#### A. Experimental results

The experimental observation of density gradient stabilization of electron-gyro scale turbulence was made in NSTX H-mode plasmas, where large density gradient variation in the core could occur as a result of large ELM events. One observation is shown in Fig. 2 where we show the waveforms of some equilibrium quantities of a NSTX H-mode plasma with  $I_p = 900$  kA and  $B_T = 4.5$  kG (shot 140620). The  $D_\alpha$  waveform shows that an ELM event occurs at about

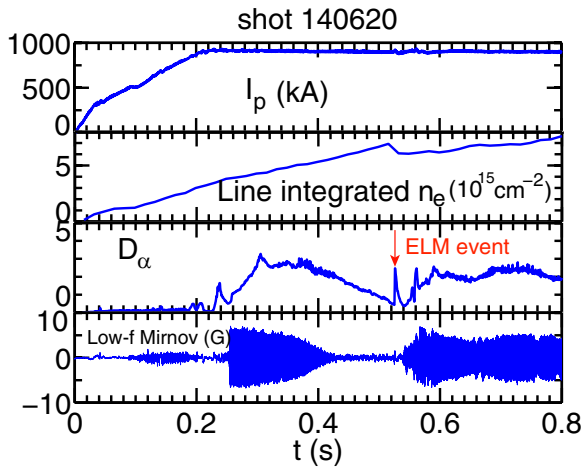


FIG. 2. An overview of shot 140620. From top panel down: plasma current, linear integrated electron density,  $D_\alpha$  emission (not calibrated), and low frequency magnetic fluctuations. The timing of an ELM event is denoted by the red arrow in the panel of the  $D_\alpha$  waveform.

$t = 524$  ms, and the line integrated electron density waveform shows a large drop following the ELM event. The ELM event occurs during plasma current flattop and has small associated low frequency MHD activity. A more detailed examination is shown in Fig. 3, where we expand the time axis around the ELM event for both  $D_\alpha$  [Fig. 3(a)] and Mirnov signal [Fig. 3(b)]. The low frequency Mirnov signal shows that no large MHD mode occurred before, during and right after the ELM. The density and temperature radial profiles measured by Multi-point Thomson Scattering (MPTS)<sup>30</sup> are plotted in Figs. 3(c) and 3(d) at  $t = 498$  ms, before the ELM, and at  $t = 532$  ms, after the ELM. The high- $k$  system measurement region, the overall radial region covered by all channels with the center of scattering location separated by  $\lesssim 1$  cm, is denoted by the shaded region in Figs. 3(c) and 3(d) from about  $R = 134$  to  $139$  cm ( $r/a \approx 0.66 - 0.77$ ). It can be seen that after the ELM, the density gradient increased significantly in the high- $k$  measurement region,

while only a small change appears in the electron temperature profile.

In Fig. 4, the upper panels show the spectrograms of the scattered signals around the ELM event ( $t = 524$  ms), where the three exact MPTS time points, i.e.,  $t = 498$ ,  $515$ , and  $532$  ms, are denoted by three colored lines in each panel. The lower panels plot the frequency spectra at these three time points for each of the five high- $k$  channels. The wavenumbers measured by the five channels correspond to  $k_\perp \rho_s$  of 11–13, 8–10, 6–9, 3–5, and 1.5–3.5 from channel 1 to 5, respectively, before the ELM. After the ELM, because of the greater refraction due to the larger density gradient, the wavenumber measured by each channel becomes larger, corresponding to  $k_\perp \rho_s$  of 14.5–16.5, 12–14, 10–12, 7–9, and 4–6 from channel 1 to 5, respectively. For each channel, the signal from collective scattering of microwave by electron density fluctuations manifests as spectral peaks at negative frequencies, which corresponds to wave propagation in the ion diamagnetic drift direction in the Lab frame. However, each channel has a Doppler frequency shift [ $f_{\text{Doppler}} = k_T V_T / 2\pi$ ,  $k_T$  is the toroidal wavenumber from ray tracing (see Fig. 1 for example), and  $V_T$  is the plasma toroidal flow velocity from charge exchange recombination spectroscopy (CHERS) measurements<sup>31</sup>] denoted by vertical lines in the lower panels of Fig. 4. After subtracting the Doppler shift, channels 1, 2, 3, and 4 show that the wave propagating direction is in the electron diamagnetic direction, which is on the right hand side of the vertical lines (although the spectral peak frequencies of channels 1 and 2 fall into the uncertainties of  $f_{\text{Doppler}}$ ), and the propagation direction is thus consistent with that of ETG modes. On the other hand, channel 5 has the spectral peak frequency of scattered signal approximately equal to  $f_{\text{Doppler}}$  at  $t = 498$  ms, and the propagation direction is uncertain. In the next step of this research, we will compare these observations with nonlinear gyrokinetic simulations coupled with a synthetic diagnostic for the scattering system to further our understanding of the propagation direction of the observed modes. We also note that the large symmetric central peaks

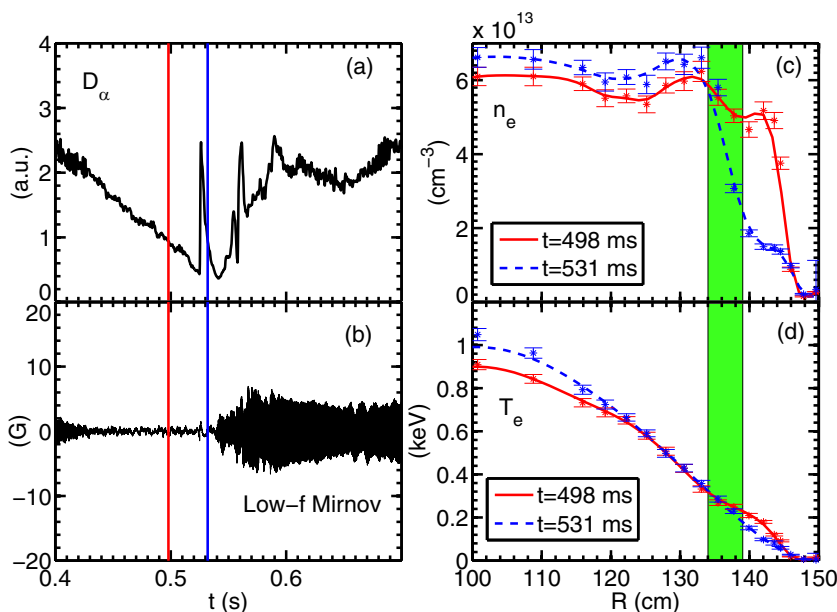


FIG. 3. Some equilibrium quantities around the ELM event occurring at 524 ms for shot 140620: (a)  $D_\alpha$  waveform; (b) low frequency Mirnov signal; (c) radial profiles of electron density at  $t = 498$  and  $532$  ms, which are before and after the ELM, respectively; (d) radial profiles of electron temperature at  $t = 498$  and  $532$  ms. The shaded regions in panels (c) and (d) denote the measuring regions of the high- $k$  system. A large change in  $L_{n_e}$  after the ELM at  $t = 524$  ms is evident.

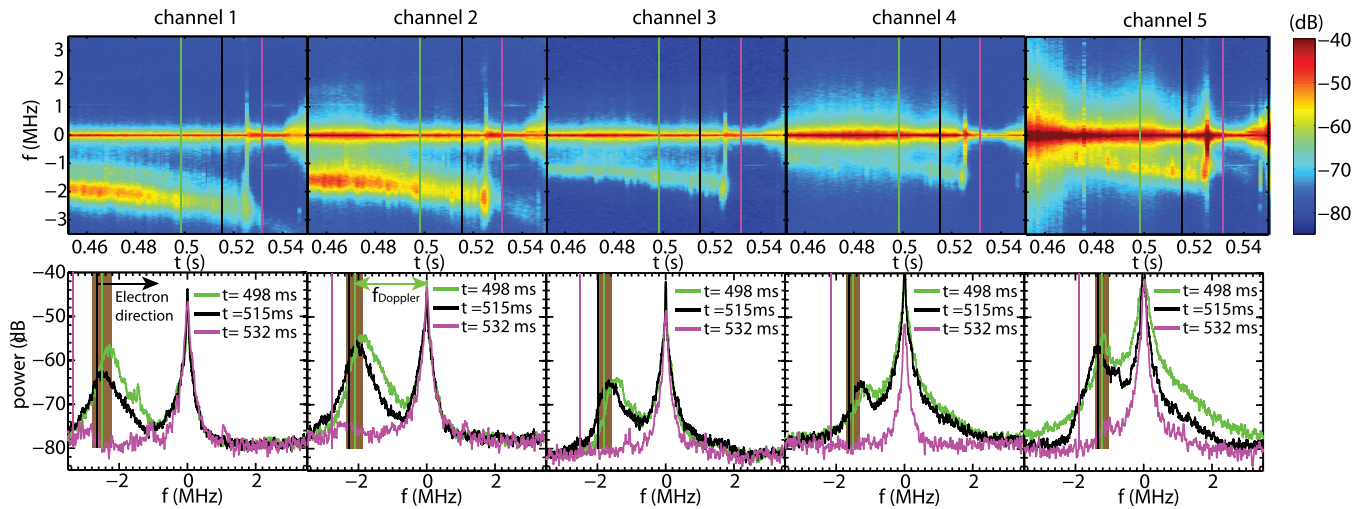


FIG. 4. Upper panels: The spectrograms of five high- $k$  channels around the ELM; Lower panels: The frequency spectra at the three exact MPTS time points around the ELM for the five high- $k$  channels. The three colored lines in the upper panels denote time points used for plotting the lower panels with the same color coding, and the three colored lines in the lower panels denote the Doppler frequencies,  $f_{\text{Doppler}} = k_{\perp} V_T / 2\pi$ , at the time points with the same color coding (Note that for clarity, only uncertainties of  $f_{\text{Doppler}}$  at  $t = 498$  ms are shown as denoted by the widths of the shaded regions). The electron direction is on the right hand side of the vertical lines in the lower panels, as shown for channel 1.

at  $f=0$  are due to the spurious reflections of the probing microwave beam. Large frequency separation of the scattering signals from the central peaks ensures accurate measurements of scattered microwave power. From Fig. 4, it can be immediately seen that although there are some variations in fluctuation power before the ELM, all channels show large reduction in measured fluctuation power after the ELM. Most notably, the scattering signals received by channels 3 and 4 are around their noise levels. However, since the wavenumber measured by each channel also changes after the ELM, further analysis is required to show the change in the wavenumber spectrum, as will be discussed below.

Figure 5 shows the  $k_{\perp}$  spectra of normalized density fluctuation in arbitrary unit at the three MPTS time points. For channels 3 and 4, which correspond to  $k_{\perp} \rho_s$  of 12.5–14.5 and 10–12 at  $t = 532$  ms, estimated upper bounds are plotted, since channels 3 and 4 have scattering signals below the noise level. The upper bounds of possible fluctuation power

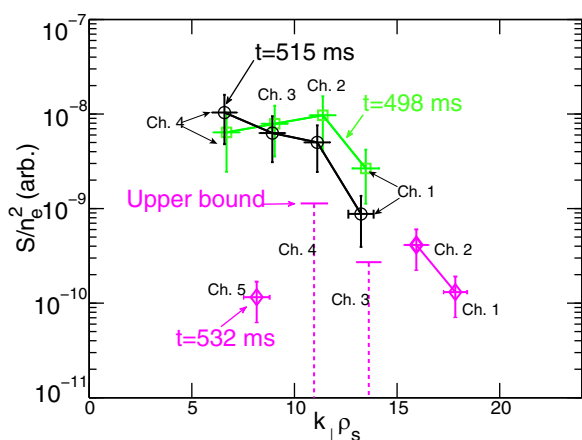


FIG. 5. The  $k_{\perp}$  spectra at the three MPTS time points ( $S$  is the spectral density). The absolute upper bounds for the density fluctuation spectral power are denoted by horizontal solid lines on the tops of vertical dashed lines.

are estimated by using the scattering signal power of channel 5 ( $k_{\perp} \rho_s$  of about 7–9), which is about three times higher than noise level, to obtain a minimum detectable scattering power (channel 5 has similar noise level as channels 3 and 4). It is clear from Fig. 5 that after the ELM ( $t = 532$  ms), the fluctuation power for  $k_{\perp} \rho_s \lesssim 15$  is reduced and the most significant reduction, more than an order of magnitude, occurs at small wavenumbers,  $k_{\perp} \rho_s \lesssim 10$ . We note that the actual reduction in spectral power in channels 3 and 4 could be more than denoted by the upper bounds. Interestingly, the fluctuation power at higher wavenumbers,  $k_{\perp} \rho_s \gtrsim 15$ , seems to be unaffected by the increase of density gradient, i.e., overlap in fluctuation power is expected if one extrapolates the  $k_{\perp}$  spectrum at  $t = 515$  ms with a power law to higher wavenumbers. However, since we have no measurements at  $k_{\perp} \rho_s > 15$  before the ELM, it is not yet possible to confirm this speculation. We also note that channel 5 is not included in the two  $k_{\perp}$  spectra before the ELM, since for those particular density profiles, its scattering location is separated more than 2 cm from those of the other four channels. However, this channel is included in the  $k_{\perp}$  spectrum at  $t = 532$  ms, since the change of density profile after the ELM leads to a better overlap of the radial scattering locations ( $\lesssim 1$  cm).

In order to demonstrate that the density gradient has the largest change in the high- $k$  measurement region, the time evolution of 10 equilibrium quantities around the ELM event are plotted at the three MPTS time points in Fig. 6. The error bars in the figure represent profile variations in the high- $k$  measurement regions. Electron temperature ( $T_e$ ), density ( $n_e$ ), the normalized electron density gradient ( $R_0/L_{n_e}$ ), and normalized electron temperature gradient  $R_0/L_{T_e}$  are obtained from the MPTS profiles.  $T_i$ ,  $Z_{\text{eff}}$ , and normalized ion temperature gradient  $R_0/L_{T_i}$  are obtained the CHERS measurement.<sup>31</sup>  $R_0$ ,  $q$ , and  $\hat{s}$  are obtained from LRDFIT (LR circuit model with Data FITting capabilities) equilibrium reconstructions constrained by magnetic pitch angle measurements from a

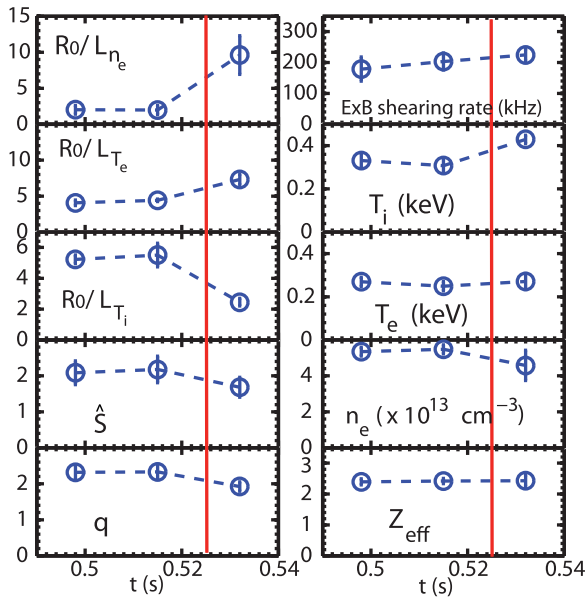


FIG. 6. Ten relevant equilibrium quantities at  $t=498$ ,  $515$ , and  $532$  ms averaged in the high- $k$  measurement locations (see main text). The timing of the ELM event is denoted by the red vertical solid lines.

motional stark effect (MSE) diagnostic.<sup>32,33</sup> The  $E \times B$  shearing rate is calculated with the Hahm-Burrell definition.<sup>34</sup> It is easy to see from Fig. 6 that the greatest change in the equilibrium quantities after the ELM is the factor of 5 increase of  $R_0/L_{n_e}$ . The next largest changes are the 60% increase in  $R_0/L_{T_e}$  and the 60% decrease in  $R_0/L_{T_i}$ . Despite the increase in the  $T_e$  gradient which drives ETG modes, the turbulence spectral power is significantly decreased as shown in Fig. 5. The decrease in  $R_0/L_{T_i}$  affects the stability of ITG modes and has small effects on the stability of either ETG or TEM modes. Indeed, as will be shown in Fig. 12, TEM modes become the most unstable ion-scale instability due to the increased  $R_0/L_{T_e}$  and  $R_0/L_{n_e}$  (Ref. 23) after the ELM. Even before the ELM, the observation of neoclassical level of ion transport (not shown) indicates that ITG modes are stabilized by geometrical and  $E \times B$  shear effects<sup>35</sup> (also see Fig. 12). In addition to changes in gradients, the 40% increase in  $T_i$  decreases  $T_e/T_i$ , which can be a destabilizing effect as seen from the first term in the “max” function in Eq. (1). However, we will show later that the density gradient change is so large that the second term in the “max” function overcomes the first term. Finally, we point out that as evident in Fig. 6, all other relevant equilibrium quantities,  $T_e$ ,  $n_e$ ,  $\hat{S}$ ,  $q$ ,  $Z_{\text{eff}}$ , and the Hahm-Burrell  $E \times B$  shearing rate show less than 25% change after the ELM.

The stabilization of the electron-scale turbulence is also found to be accompanied by an improvement in plasma confinement. The transport analysis was carried out with a time dependent tokamak transport and data analysis code (TRANSP) (Ref. 36) using measurements from MPTS, CHERS, and the equilibrium from LRDFIT reconstruction. Figure 7 plots electron thermal diffusivity,  $\chi_e$ , as a function of  $R$  before the ELM at  $t=498$  and after the ELM at  $t=532$  ms, where a factor of about two reduction in  $\chi_e$  can be seen in the high- $k$  measurement region. (We note that the uncertainty in  $\chi_e$  in Fig. 7 is mainly due to uncertainties in

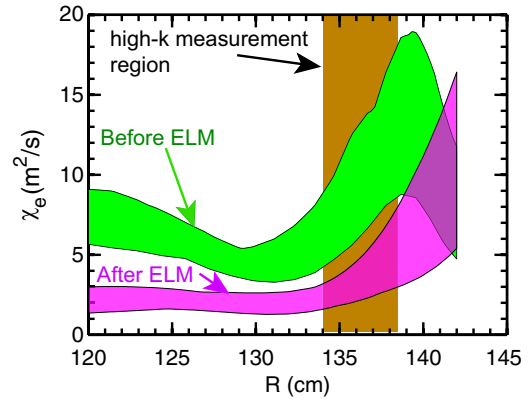


FIG. 7. The electron thermal diffusivity as a function of  $R$  before the ELM at  $t=498$  (green) and after the ELM at  $t=532$  (magenta) with the shaded region denoting the high- $k$  measurement regions.

ohmic heating and measured kinetic profiles). This correlation suggests that the reduction in the longer wavelength modes,  $k_{\perp} \rho_s < 10$ , may be responsible for the improvement in the electron thermal transport. We finally note that ion transport remains at the neoclassical level before and after the ELM event.

## B. Comparisons with gyro-kinetic simulations

Both linear and nonlinear gyrokinetic simulations were carried out using the experimental profiles both before and after the ELM event. The linear stability analysis was performed with the GS2 gyrokinetic code.<sup>21</sup> GS2 is an initial value gyrokinetic code which, in its linear mode, finds the fastest growing mode for a given pair of poloidal and radial wavenumbers. Nonlinear simulations were performed with the Eulerian gyrokinetic code GYRO (Refs. 19 and 37). Here, we present linear stability analysis in Sec. III B 1 and nonlinear simulation results in Sec. III B 2. Both linear and nonlinear simulations use local Miller equilibria,<sup>38</sup> which allow us to isolate the effects of individual parameters.

### 1. Linear stability analysis

In Fig. 8, we plot the linear growth rate and mode frequency of electron-scale modes as a function of poloidal wavenumber ( $k_{\theta}$ ) before the ELM at  $t=498$  ms and after the ELM at  $t=532$  ms at  $R=133.5$  cm, which is around the inner edge of the high- $k$  measurement region (This location is chosen to show how ETG growth rate spectrum changes before and after the ELM, while ETG can be stable at other locations in the high- $k$  region as will be shown later). Since the mode frequency ( $\omega$ ) is negative (see Fig. 8(b)), the unstable modes propagate in the electron diamagnetic drift direction both before and after the ELM. The corresponding mode structures have even parity in electrostatic potential and odd parity in parallel magnetic potential (not shown). Furthermore, the calculated instability survives when electron beta is set to zero and is found to be driven by electron temperature gradient. Thus, we are confident that the calculated unstable modes are ETG modes. From Fig. 8(a), we can see that the peak linear growth of the unstable ETG modes is both decreased after the

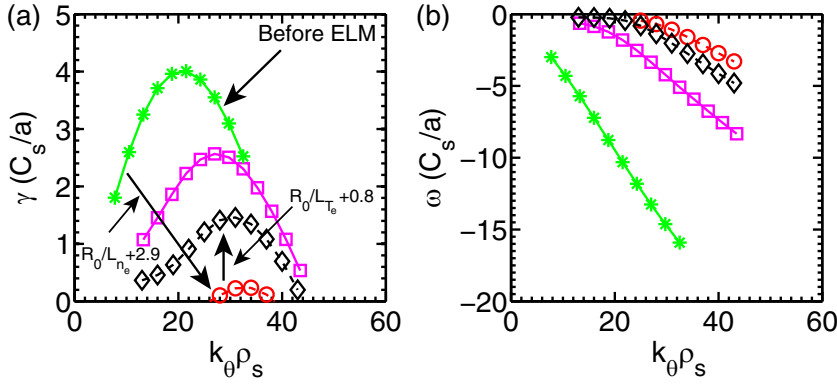


FIG. 8. (a) Linear growth rate,  $\gamma$ , and (b) mode frequency,  $\omega$ , of ETG modes before the ELM at  $t = 498$  ms (green asterisks) and after the ELM at  $t = 532$  ms (magenta open squares) calculated with GS2 code at  $R = 133.5$  cm (around the inner edge of the high- $k$  measurement region) using local Miller equilibrium. Note that modes with  $\omega < 0$  propagate in the electron diamagnetic drift direction. Parametric scans in  $R_0/L_{n_e}$  and  $R_0/L_{T_e}$  based on “before ELM” parameters are also shown:  $R_0/L_{n_e}$  increased by 2.9 (red open circles);  $R_0/L_{n_e}$  and  $R_0/L_{T_e}$  increased by 2.9 and 0.8 simultaneously (black diamonds).

ELM and shifted to larger  $k_\theta$ . Therefore, we expect the ETG-induced transport will decrease after the ELM, which will be demonstrated by nonlinear ETG simulation results shown in Sec. III B 2. We also investigate what parametric changes after the ELM lead to the change of the growth rate spectrum. Based on the “before ELM” parameters, we increase density gradient to  $R_0/L_{n_e} + 2.9$  to match the “after ELM” density gradient, and it is obvious in Fig. 8 that the resulting growth rates and mode frequencies are very different from the “before ELM” case: the growth rates are much smaller, the peak growth rate is shifted to higher wavenumber, and the mode frequencies are also smaller. Thus the trend of changing in the growth rate spectrum seen after the ELM is consistent with the effect of density gradient increase. However, the growth rate spectrum from increasing density gradient alone does not match the “after ELM” growth rate spectrum. Since ETG also increased after the ELM, linear calculation was also carried out with density gradient and ETG increased to  $R_0/L_{n_e} + 2.9$  and  $R_0/L_{T_e} + 0.8$ , respectively, to match the “after ELM” parameters. Seen in Fig. 8, the resulting linear growth rates are now closer to but still smaller than those of “After ELM”, and we expect other equilibrium quantity changes after the ELM to further destabilize ETG modes and increase the growth rate. Nevertheless, it is obvious that density gradient alone has very strong stabilization effect on ETG modes and could significantly increase the stability threshold.

Since Fig. 8 only shows ETG stability at one radial location, here we present the stability of ETG modes throughout the high- $k$  measurement region by comparing calculated critical temperature gradient and measured temperature gradient. We will show that the observed density gradient stabilization is in good agreement with our stability analysis. We follow the procedure in Ref. 24 to find the critical temperature gradient: growth rates of a range of unstable poloidal wavenumbers are calculated with several different temperature gradients, and linear extrapolation of the growth rate of the most unstable mode determines the critical temperature gradient. In Fig. 9, the critical ETG in the high- $k$  measurement region were calculated using GS2 and are plotted for the three MPTS time points together with measured  $T_e$  gradient profile. Figure 9 clearly shows that at the time points before the ELM, i.e., 498 ms (a) and 515 ms (b), the measured  $T_e$  gradients are larger than the critical  $T_e$  gradients in most of the high- $k$  measurement region. However, at  $t = 532$  ms (c), after

the ELM, the critical  $T_e$  gradient from GS2 calculations is much larger than the measured  $T_e$  gradient for most of the high- $k$  measurement region, i.e., ETG modes are linearly stable, which is able to explain the observed large reduction of spectral power for  $k_\perp \rho_s < 10$  at  $t = 532$  ms as shown in Fig. 5. We note that due to the small size of the existing ETG unstable region, where  $(a/L_{T_e})_{\text{measured}} > (a/L_{T_e})_{\text{critic,GS2}}$ , in Fig. 9(c), and corresponding smaller linear growth (see Fig. 8(a)), the ETG fluctuations in this unstable region may not be large enough to explain the possible unaffected spectral power for  $k_\perp \rho_s \gtrsim 15$  in Fig. 5. In order to show that the density gradient increase is responsible for the large increase of critical  $T_e$  gradient in Fig. 9(c), critical  $T_e$  gradients calculated with  $R_0/L_{n_e}$  decreased by 3, 4.5, and 6 units are also plotted in Fig. 9(c). It is clear that  $(R_0/L_{n_e} - 3)$  leads to significantly lowered critical  $T_e$  gradients in the high- $k$  measurement region. However, while the decreases to  $(R_0/L_{n_e} - 4.5)$  and  $(R_0/L_{n_e} - 6)$  lead to further reduction of critical  $R_0/L_{T_e}$  at  $R > 135.5$  cm, only small change in critical  $R_0/L_{T_e}$  is observed at  $R \lesssim 135$  cm, which is consistent with the first

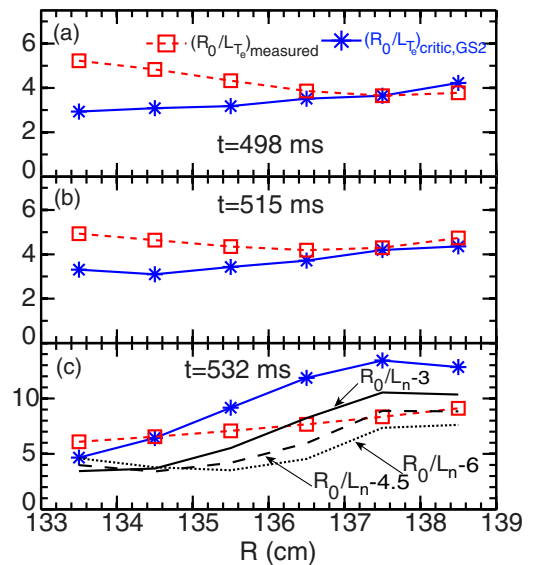


FIG. 9. The critical  $T_e$  gradients calculated by GS2,  $(R_0/L_{T_e})_{\text{critic,GS2}}$  (asterisks) in comparison with the measured temperature gradient,  $(R_0/L_{T_e})_{\text{measured}}$  (open squares) in the high- $k$  measurement region: (a) at  $t = 498$  ms; (b)  $t = 515$  ms; and (c)  $t = 532$  ms. Additional lines in (c) denote  $(R_0/L_{n_e})_{\text{critic,GS2}}$  calculated with  $(R_0/L_{n_e} - 3)$  (solid line),  $(R_0/L_{n_e} - 4.5)$  (dashed line), and  $(R_0/L_{n_e} - 6)$  (dotted line).

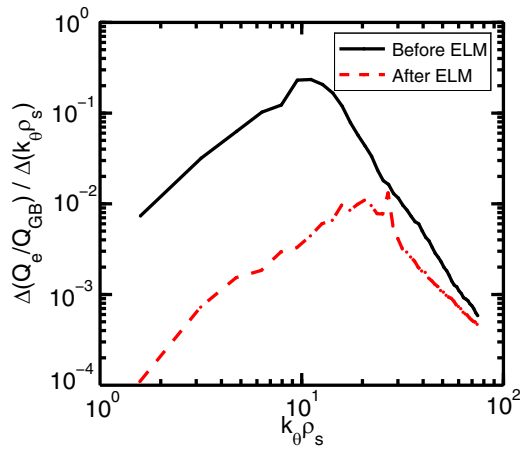


FIG. 10. Fractional electron heat flux as a function of  $k_\theta \rho_s$  for “before ELM” at  $t = 498$  ms (black solid line) and “after ELM” at  $t = 532$  ms (red dashed line) at  $R = 133.5$  cm.

term in the “max” function on the RHS of Eq. (1) dominating the critical  $R_0/L_{Te}$  as the second density gradient term becomes sufficiently small.

## 2. Nonlinear results

Here, we present the results from local nonlinear ETG simulations for both “before ELM” and “after ELM” cases. These local nonlinear simulations use local Miller equilibria and plasma parameters derived from measured experimental profiles, kinetic electrons, and ions with real mass ratio ( $M/m_e = 3600$ ), collisions, shear and compressional magnetic perturbations (although we found that calculated transport is dominantly electrostatic), and toroidal flow and flow shear. All nonlinear simulations used a perpendicular box of  $L_x \times L_y \approx 6 \times 4 \rho_s$ , 48 complex toroidal modes, 192 radial grid points, 8 energies, 8 pitch angles, and 10 parallel mesh points ( $\times 2$  signs of parallel velocity). Numerical convergence of the simulations has been verified by following the procedure outlined in Ref. 20.

Figure 10 shows the fractional electron heat flux versus  $k_\theta \rho_s$  (at  $R = 133.5$  cm), where it is obvious that the peak of the fractional electron heat flux is not only dramatically decreased after the ELM but also shifted to larger  $k_\theta$  modes. We want to emphasize that this change in the fractional electron heat flux spectrum is consistent with the change in linear growth rates observed in Fig. 8.

The comparison with experimental electron heat flux,  $Q_e$ , is shown in Fig. 11(a), where the experimental  $Q_e$  calcu-

lated using the same TRANSP analysis as used for Fig. 7 is shown as solid blocks whose height denotes the experimental uncertainty (mainly due to uncertainties in ohmic heating and measured kinetic profiles) and whose width denotes the range of density gradient from  $R = 133.5$  cm to  $R = 135.5$  cm, about the inner half of the high- $k$  measurement region where we have performed nonlinear simulations. Note that after the ELM, both the density gradient and its range increased significantly. It is obvious from Fig. 11(a) that the experimental  $Q_e$  decreases by about 1 MW after the ELM. This decrease in  $Q_e$  is mostly due to the decrease in electron and ion coupling after the ELM, and larger radiation loss and  $dW_e/dt$  ( $W_e$  is the electron thermal energy) after the ELM also contribute. As shown in Fig. 11, the simulations based on “before ELM” and “after ELM” parameters show similar trend in change of  $Q_e$  as observed in the experiment: a significant reduction of  $Q_e$  after the ELM. In order to demonstrate that the density gradient is the responsible parameter, nonlinear simulations with scans in density gradient were carried out: density gradient was increased by 1.5 and 2 times based on the “before ELM” parameters and reduced by 1/3 and 2/3 based on the “after ELM” parameters. The predicted  $Q_e$ ’s from these scans as shown in Fig. 11(a) clearly demonstrate the strong stabilizing effect of density gradient to the ETG-induced electron thermal transport. For instance, the scan based on the “after ELM” parameters, a factor of 3 reduction in density gradient can result in an order of magnitude increase in  $Q_e$ . Similar trend is also seen in the scan based on the “before ELM” parameters.

Noticing that the nonlinear ETG simulations based on nominal experimental parameters constantly underpredict  $Q_e$  comparing to the experimental values, we investigated the sensitivity of the ETG-induced transport by increasing ETG by 20% and 40%, and the corresponding predicted  $Q_e$ ’s are shown in Fig. 11(b). It can be seen that the ETG-induced transport is quite sensitive to ETG before the ELM, the predicted  $Q_e$  is more than doubled just by increasing ETG by 20%, and increasing ETG by 40%, the predicted  $Q_e$  is already at the upper bound of the experimental value. On the other hand, after the ELM, increasing ETG by 40% still cannot match the experimental values. Thus, an additional mechanism is needed to account for the discrepancy. Indeed, Fig. 12(a) shows that ion scale instabilities are unstable both before and after the ELM. However, before the ELM, the  $E \times B$  shear rate (calculated using Waltz-Miller definition<sup>39</sup>) is more than twice larger than the peak growth rate; and after the ELM, the peak growth rate is about 40% higher than the  $E \times B$

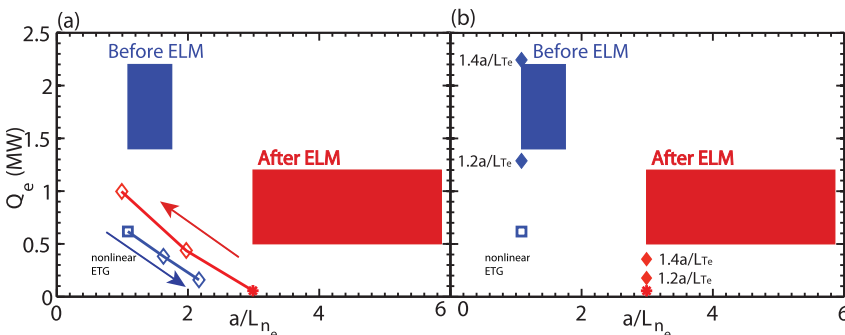


FIG. 11. (a) Experimental electron heat flux from TRANSP analysis (solid rectangles) and calculated  $Q_e$  from nonlinear GYRO simulations (asterisk and open square) before the ELM ( $t = 498$  ms) and after the ELM ( $t = 532$  ms). Parametric scans (open diamonds) in density gradient based on “before ELM” and “after ELM” parameters are also shown. (b) The same as (a), except that parametric scans are in ETG.

shearing rate. From Fig. 12(b), we can see that ITG mode is the most unstable mode before the ELM, but TEM becomes most unstable mode after the ELM, which is consistent with well-known density gradient destabilization of TEM.<sup>23</sup> Therefore, we expect that TEM could contribute to electron thermal transport. Indeed, without  $E \times B$  shear, a preliminary *local* nonlinear TEM simulation produces  $\sim 30$  MW of electron heat flux. Restarting the same simulation using the experimental level of  $E \times B$ , shearing rate produced electron heat flux is dramatically reduced near the experimental level ( $\sim 0.5 - 1.2$  MW). However, this result has not been verified for numerical convergence. Furthermore, given the large eddy size of TEM turbulence and the small  $a/\rho_s$  of NSTX (typically 100 for the plasmas presented in the paper), we expect that non-local effects due to variations in equilibrium profile will alter the quantitative solution. For example, the strongly unstable TEM at  $R = 135.5$  cm can easily spread to  $R = 133.5$  cm, which is only  $3\rho_i$  away and can affect transport there. Additional simulations are underway to investigate the ion scale turbulence and will be reported elsewhere.

#### IV. STUDY OF ELECTRON COLLISIONALITY DEPENDENCE

The normalized confinement time in NSTX is found to strongly scale with electron collisionality,  $B_T \tau_E \propto \nu_e^{*-1}$ .<sup>11</sup> As future spherical tokamaks such as NSTX-Upgrade<sup>40</sup> and a candidate for Fusion Nuclear Science Facility<sup>41</sup> will be operating at much lower  $\nu_e^*$  than NSTX, the performance for these devices strongly depends on whether the observed collisionality scaling remains valid in the lower collisionality regime, and understanding the underlining mechanisms of this scaling is crucial for answering this question. In the literature, ETG and microtearing turbulence are both proposed as potential mechanisms, which could drive anomalous electron thermal transport in spherical tokamaks.<sup>12,17,37,42</sup> In particular, over a range of collisionality, the microtearing mode can be destabilized with increasing collisionality.<sup>6</sup> Recent nonlinear simulations show that the predicted transport,  $\chi_e \sim \nu_e^{e/i}$ , qualitatively follows the linear trend and is consistent with the experimental confinement scaling.<sup>37</sup> However, if microtearing turbulence were indeed responsible for the observed confinement scaling of the present spherical tokamaks, it is still unknown whether it would be dominant as collisionality gets into the lower collisionality regime of future spherical tokamaks (Refs. 40 and 41), and ETG turbulence may become a competing source of anomalous electron thermal transport. On the other hand, although the linear ETG instability should not be affected by electron collisionality as long as  $\omega \gg \nu_e^{e/i}$ , the situation is more complicated nonlinearly, and an analytical analysis in Ref. 43 shows that the collisional damping of ETG-mode-driven zonal flow could lead to stronger ETG turbulence/transport as collisionality increases, which is consistent with the experimental scaling. Furthermore, this dependence of ETG turbulence on collisionality has been observed in particle-in-cell gyrokinetic simulations.<sup>44</sup> Given the potentially important role of ETG turbulence in present and future ST's, we designed and carried out experiments with the aim to measure the depend-

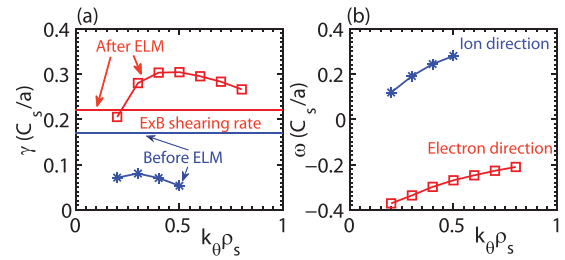


FIG. 12. (a) Ion scale linear growth rates before and after the ELM evaluated at  $R = 135.5$  cm together with the corresponding local  $E \times B$  shearing rates (horizontal lines); (b) Mode frequencies before and after the ELM evaluated at  $R = 135.5$  cm. Ion direction and electron direction correspond to  $\omega > 0$  and  $\omega < 0$ , respectively.

ence of electron-scale turbulence on  $\nu_e^*$  with  $\rho_e$ ,  $\beta_e$ , and  $q_{95}$  kept approximately constant. One important feature of the plasmas used in the experiments is that they are of low electron beta (locally in the high- $k$  measurement region),  $\beta_e \approx 2\%$ , which has stabilizing effect on microtearing instability.<sup>6</sup> Indeed, the stabilization of microtearing instability has been confirmed by linear gyrokinetic analysis. Thus, we are able to remove the effects of microtearing from the experiment.

#### A. Experimental results

The collisionality scan was carried out following an established experimental procedure in NSTX (Ref. 11) by varying  $B_T$  and  $I_p$  simultaneously with constant  $B_T/I_p$  and keeping density approximately constant. The low collisionality shots have  $B_T = 4.5$  kG and  $I_p = 900$  kA, and the high collisionality shots have  $B_T = 3.5$  kG and  $I_p = 700$  kA. An overview of two shots (one of high collisionality and one of low collisionality) used in the analysis are shown in Fig. 13. The difference in  $I_p$  between the two shots can be seen in top panel. From the next two lower panels, it is clear that the two shots have similar line integrated density and  $D_x$  waveforms are also similar. It is also obvious from the lowest panel in

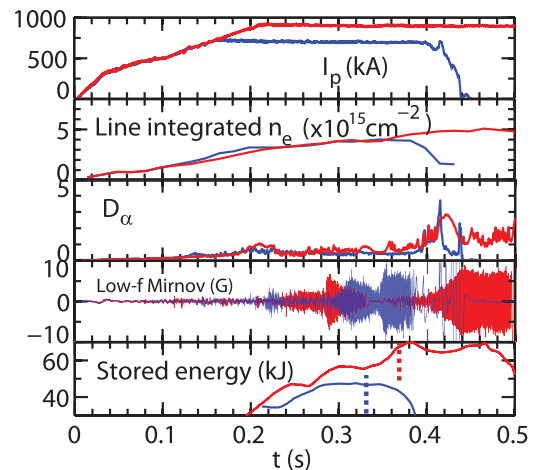


FIG. 13. Overview of a low collisionality shot (waveforms in red) and a high collisionality shot (waveforms in blue). From top panel down: plasma current, line integrated electron density,  $D_x$  emission (not calibrated), low frequency magnetic fluctuations, and plasma stored energy. The two colored vertical thick dashed lines in the lowest panel denote the times of interest for analysis with the same color coding as the waveforms.

Fig. 13 that the low collisionality shot has higher stored energy at the time of interest than the high collisionality shot (the dashed vertical lines in the lowest panel denote the time of interest), which is consistent with the observed confinement scaling with collisionality. However, at the time of interest, the high collisionality shot has higher low frequency MHD activity due to an  $n = 1$  magnetic island. This island does not overlap with the high- $k$  measurement region (about  $R = 132$  cm to 138 cm). Furthermore, the density perturbation in the high- $k$  measurement region due to the island is found to be only about 5% evaluated with a far infrared (FIR) interferometer,<sup>45</sup> and thus we do not expect it to affect the density gradient used in our numerical calculations. We also note that the stored energy of the high collisionality shot is not affected by the  $n = 1$  magnetic island after it started to grow at around  $t = 290$  ms, and this rotating MHD mode appears not to significantly alter the overall plasma confinement until it starts to lock at about 385 ms.

In order to keep local  $\rho_e$  and  $\beta_e$  constant in the collisionality scan, we need to keep  $T_e/B^2$  locally constant, i.e., the  $T_e$  profiles have to match after normalized to  $B^2$ , where  $B$  is the total local magnetic field strength. Figure 14(a) plots the  $T_e$  profiles at  $t = 367$  ms for the two low collisionality shots (141007 and 141040) and at  $t = 332$  ms for the two high collisionality shots (141031 and 141032). The collisionality variation almost exclusively comes from changes in  $T_e$ , which can be seen in Fig. 14(a): the low collisionality shots have higher  $T_e$  in the high- $k$  measurement region than the high collisionality shots (density variation is small between the high and low collisionality shots). The normalized  $T_e/B^2$  profiles are shown in Fig. 14(b), where they show good overlap from  $R = 132$  cm to 145 cm, and, of course, also in the high- $k$  measurement region. We note that  $B$  profiles used to calculate  $T_e/B^2$  are from LRDFIT equilibrium reconstructions constrained by MSE measurements.<sup>32,33</sup>

Figure 15 plots the local  $\rho_e$  and  $\beta_e$ ,  $q_{95}$ , and normalized energy confinement time,  $B_T\tau_E$ , as a function of local electron collisionality,  $\nu_e^*$ . The local values are the mean values evaluated in the high- $k$  measurement region. It is clear from Figs. 15(a)–15(c) that while  $\nu_e^*$  varies by about a factor of 2.5,  $\rho_e$ ,  $\beta_e$ , and  $q_{95}$  are kept relatively constant with less than 15% variation. As shown in Fig. 15(d), the normalized confine-

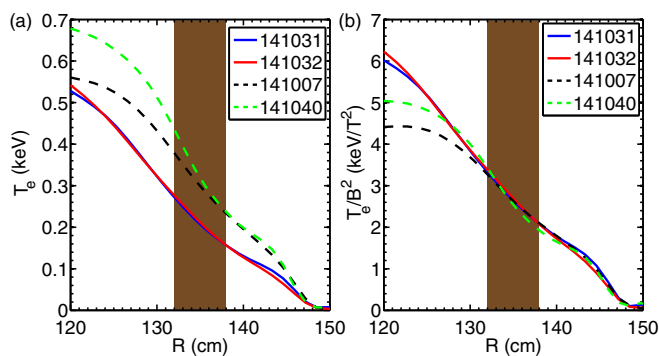


FIG. 14. (a)  $T_e$  profiles measured by MPTS at times of interest for the 4 shots used in the analysis ( $t = 367$  ms for the low collisionality shots 141007 and 141040;  $t = 332$  ms for the high collisionality shots 141031 and 141032); (b) Normalized  $T_e/B^2$  profiles for the 4 shots. The shaded regions in the figures denote the high- $k$  measurement region.

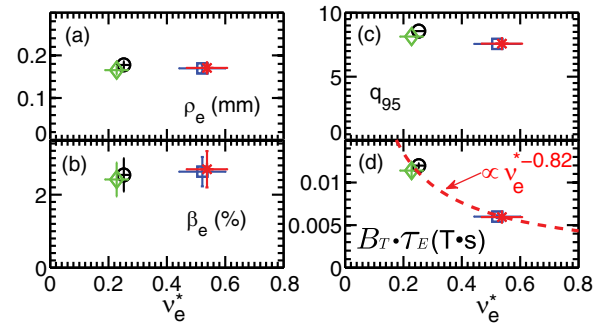


FIG. 15. (a) Local electron gyroradius,  $\rho_e$ , (b) local electron beta,  $\beta_e$ , (c)  $q_{95}$ , (d) normalized energy confinement time,  $B_T\tau_E$ , all as a function of electron collisionality,  $\nu_e^*$  for shots 141031 (blue square), 141032 (red asterisks), 141007 (black circle), and 141040 (green diamond). The local values shown in (a) and (b) are the mean values in the high- $k$  measurement region. The vertical and horizontal error bars denote the variation of corresponding quantities in the high- $k$  measurement region (applicable to  $\rho_e$ ,  $\beta_e$ , and  $\nu_e^*$ ). The red dashed line in (d) denotes a best power law fit to the normalized confinement time versus collisionality, which gives  $\nu_e^{*-0.82}$ .

ment time,  $B_T\tau_E$ , decreases as collisionality increases, and fitting the data to a power law,  $\nu_e^{*\alpha}$ , yields  $\alpha = -0.82$ , which is in agreement with the previous result of  $\alpha = -0.92$ .<sup>11</sup>

Figure 16 shows the change of electron-scale turbulence wavenumber spectrum as collisionality is varied, where the normalized turbulence spectral power is plotted as a function  $k_{\perp}\rho_s$ . It seems that an anti-correlation between measured turbulence spectral power and collisionality exists for  $k_{\perp}\rho_s > 9$ . However, the collisionality dependence of the turbulence spectra at  $k_{\perp}\rho_s < 9$  is more complicated, and one low collisionality shot (green diamond) has even smaller spectral power than the high collisionality shots in this wavenumber range. The reason for this spectral difference between the two nominally similar low collisionality shots, 141007 and 141040, may be seen qualitatively by examining their corresponding ETG mode linear growth rate and  $E \times B$  shearing rate, which are plotted in Fig. 17. The  $E \times B$  shearing rate in shot 141040 (Fig. 17(b)) is about 2 times higher than shot 141007 shown in Fig. 17(a). On the other hand, although the two shots have similar linear growth rate at  $k_{\theta}\rho_s > 4$ , the growth rate for shot 141040 is significantly smaller at  $k_{\theta}\rho_s <$

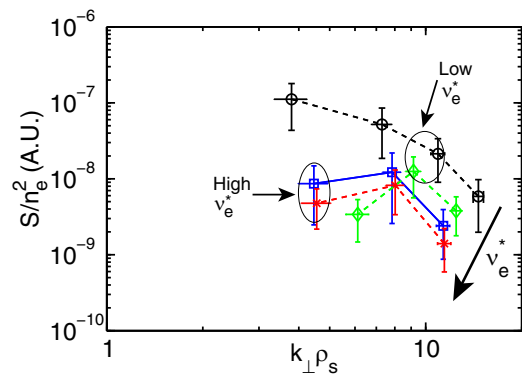


FIG. 16. The  $k_{\perp}$  spectra in arbitrary unit (normalized to  $n_e^2$  and  $S$  is the spectral density calculated using the total scattered power in the spectra of each channel) for shots 141031 (blue square), 141032 (red asterisks), 141007 (black circle), and 141040 (green diamond). The first 2 shots are of high collisionality and the latter 2 shots are of low collisionality. The direction of increase of collisionality is denoted by a black arrow.

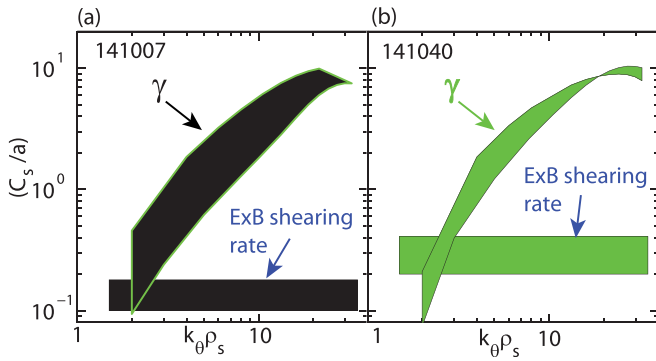


FIG. 17. (a) The range of linear growth rate and  $E \times B$  shearing rate for shot 141007; (b) The same as (a), but for shot 141040. The linear growth rates are shown for the radial region of  $R = 135.5$  to  $137.5$ , the more unstable half of the high- $k$  measurement region for ETG instability, which we expect to dominate the contribution to the scattered signal from the high- $k$  scattering system.

3 than shot 141007. The smaller growth rate at smaller wavenumbers of shot 141040 in combination with its larger  $E \times B$  shearing rate may lead to a more significant  $E \times B$  shear quenching of longer wavelength modes<sup>46</sup> than shot 141007, given its larger growth rate and smaller  $E \times B$  shearing rate. Although the comparison of linear growth rate and  $E \times B$  shearing rate seems to be qualitatively consistent with experimental observation, a quantitative answer has to be obtained from nonlinear simulations, which will be addressed in a future paper.

## B. Collisionality dependence from linear stability analysis

Here, we focus on the effect of collisionality on linear properties of ETG modes. We have previously pointed out that the ETG instability should not be affected by collisionality as long as  $\omega \gg \nu_{ei}$ . This is indeed what we found in linear stability analysis. Figure 18(a) plots the linear growth rates as a function of  $k_{\theta}\rho_s$  calculated for a low collisionality shot and a high collisionality shot at the center of the high- $k$  measurement regions together with linear growth rates from scans in  $\nu_{ei}$  ( $\nu_{ei} = \nu_{ei}^0/Z_{eff}$  as used in Ref. 6) and other param-

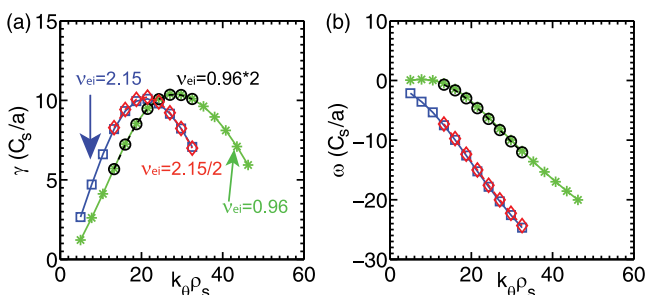


FIG. 18. Comparisons of linear growth rates (a) and mode frequencies (b) of a low collisionality shot 141040 (asterisks) and a high collisionality shot 141031 (open square) using Miller local equilibrium at  $R = 135.5$  cm (for the low collisionality shot) and  $R = 135$  cm (for the high collisionality shot). Note that growth rates and mode frequencies from collisionality scans are also shown, where collisionality is halved (open diamond)/doubled (open circle) based on high/low collisionality shot parameters to approximately match that of the low/high collisionality.

eters kept constant. It is obvious that increasing (decreasing)  $\nu_{ei}$  based on the low (high)  $\nu_{ei}$  shot parameters changes neither the linear growth rate or mode frequency. Thus, the difference in linear property between the two shots stems from some other parameters. Table I compares some relevant parameters of the two shots at  $R = 135.5$  cm. We note that in addition to  $\nu_{ei}$ , density gradient,  $a/L_{ne}$  and  $q$  are also quite different. Figures 19(a) and 19(b) shows the effect of  $a/L_{ne}$  and  $q$  on the linear growth rate, respectively, where we reduce  $a/L_{ne}$  and  $q$  from those of a low collisionality shot (141040) to match those of the high collisionality shot (141031). It can be seen that reducing  $a/L_{ne}$  or  $q$  increases the growth rate at smaller wavenumbers ( $k_{\theta}\rho_s < 20$ ) to almost match those of the high collisionality shot and also moves the peak growth rate to smaller wavenumber. We note that the effect of density gradient on growth rate shown in Fig. 19 is consistent with what is shown Fig. 8, except that the change in density gradient is much larger in Fig. 8. We also note that although we found no collisionality dependence in linear analysis, the collisionality effect on ETG turbulence shown in Ref. 43 is a pure nonlinear effect. Thus, nonlinear simulations have to be performed to investigate the role of zonal flow damping.

## C. Nonlinear results

Here, we first present nonlinear simulation results of collisionality dependence based on the low and high collisionality shots. The local Miller equilibrium parameters at the center of the high- $k$  measurement region were used in the simulations, and the results are compared with experimental  $Q_e$  from power balance analysis using TRANSP. Figure 20 plots  $Q_e$  from experiments and simulations as a function of electron collisionality. Note that the experimental  $Q_e$  is shown as solid rectangles whose height denotes the experimental errorbars, which are mainly due to the uncertainties in Ohmic heating power. From Fig. 20(a), it is clear that the base cases using local equilibrium quantities of both shots predicted much smaller  $Q_e$ 's than experiments. Furthermore, the parametric scans in  $\nu_{ei}$  demonstrate very weak dependence on electron collisionality. Note that the scans in  $\nu_{ei}$  have been performed based on parameters of shot 141031 by reducing  $\nu_{ei}$  to 1/2 and 1/4 of its original value, and similar scans have also been performed based on parameters of shot 141040 using  $\nu_{ei}$  with 2 and 4 times of its original value. These scans show that the final nonlinear saturated turbulence level depends very weakly on collisionality, which is clearly different from the analytic result in Ref. 43. It may be the case that since the amount of collisionality is already small in these plasmas, and increasing/reducing it by a factor 2 or 4 does not change the zonal flow level significantly. Further scans in collisionality are needed to clarify this issue. Another obvious result shown in Fig. 20(a) is that the  $Q_e$  predicted for shot 141040 is significantly smaller than shot 141031 of higher collisionality. We point out that this is consistent with the fact that the linear growth rates of shot 141040 are smaller than those of shot 141031 at lower wavenumbers,  $k_{\theta}\rho_s < 20$  (Fig. 18) and long wavelength fluctuations are more important in driving transport. If the difference in linear growth rates are indeed carried over to

TABLE I. Some relevant equilibrium quantities at  $R = 135.5$  cm for the low collisionality shot (141040) and  $R = 135$  cm for the high collisionality shot (141031) as used in the GS2 simulations. Note that here  $\beta_{e,GS2}$  is defined using the  $B_T$  at the center of the last closed flux surface which is also used for  $\beta'_{GS2}$ .

shot	$r/a$	$T_i/T_e$	$q$	$\hat{s}$	$\hat{s}/q$	$a/L_{T_e}$	$a/L_{n_e}$	$Z_{eff}$	$\nu_{ei} (C_s/a)$	$\beta_{e,GS2}$	$\beta'_{GS2}$
141040	0.66	1.12	1.92	1.23	0.64	4.64	2.36	1.19	0.96	1.2%	-0.27
141031	0.6	1.18	1.54	1.04	0.672	4.56	1.64	1.22	2.15	1.4%	-0.27

nonlinear results, we would expect that the difference in predicted  $Q_e$  be more affected by the density gradient and  $q$  rather than collisionality, as can be seen from the linear results shown in Fig. 19.

We also investigated the sensitivity of predicted transport to ETG by varying  $a/L_{T_e}$ , and the results are shown in Fig. 20(b). It can be seen that although it is possible to significantly enhance  $Q_e$  by increasing  $a/L_{T_e}$  by 40%, the absolute values of  $Q_e$  still do not match experimental ones, particularly for the low collisionality shot 141040. Thus, these local nonlinear ETG simulations seem unable to account for observed electron thermal transport at the evaluated radial locations. Of course, these simulations were carried out at just one radial location for each shot, and given the profile variations in the high- $k$  measurement region, results could be different elsewhere.

Table II shows the ranges of some relevant equilibrium quantities in the high- $k$  measurement regions (about  $R = 133.5$  to  $137.5$  cm for shot 141040 and about  $R = 133$  to  $137$  cm for shot 141031). Most notably, the density gradient can vary more than a factor of 3 in the high- $k$  measurement region. Furthermore,  $\hat{s}$  and  $E \times B$  shearing rate can also vary for a factor of 2-3. Motivated by this observation, we performed multiple local nonlinear ETG simulations in the high- $k$  measurement region using general equilibrium (from LRDFIT) instead of the Miller local equilibrium, and kinetic profiles taken from TRANSP. Figures 21(a) and 21(b) show the predicted  $Q_e$  radial profile together with the experimental  $Q_e$  profiles in the high- $k$  measurement range for the low collisionality shot 141040 and the high collisionality shot 141031, respectively. A common feature shared by Figs. 21(a) and 21(b) is that the predicted  $Q_e$  has large variation, more than an order of magnitude, in the high- $k$  measurement

region. On the other hand, the maximum value of predicted  $Q_e$  for shot 141040 in Fig. 21(a) is much smaller than the experimental level of  $Q_e$ , however Fig. 21(b) shows that the maximum value of predicted  $Q_e$  at  $R = 133$  cm for shot 141031 is very close to the experimental level. There is no doubt that due to the sensitivity of predicted  $Q_e$  to  $a/L_{T_e}$  observed in Fig. 20(b), a small increase in  $a/L_{T_e}$  should be able to increase the predicted  $Q_e$  to match the experimental level. However, what is more interesting is the more-than-an-order-of-magnitude variation of the predicted  $Q_e$  in the high- $k$  measurement region.

Here, we will show that the density gradient is strongly anti-correlated with the predicted  $Q_e$ . This can be seen clearly from the radial profiles of the predicted  $Q_e$  and density gradient,  $a/L_{n_e}$ , plotted in Figs. 22(a) and 22(b) for the same simulations in Fig. 21. Note that the density gradient profiles are totally different between the two shots, where the  $a/L_{n_e}$  increases toward larger radius in Fig. 22(a) while decreases in Fig. 22(b). At the same time, the predicted  $Q_e$  exhibits reversed trend against the density gradient, for example, decreasing toward larger radius in Fig. 22(a). In addition to this prominent anti-correlation relationship, we also found that the flat radial region for  $a/L_{n_e}$  ( $R > 135$  cm) in Fig. 22(a) also corresponds to the flat radial region for  $Q_e$ , which further supports the strong dependence between the two quantities. The anti-correlation between the predicted  $Q_e$  and  $a/L_{n_e}$  is more clearly shown in Fig. 22(c) where the two quantities are plotted against each other and a monotonic relationship between them is clear. We note that although the density gradient changes only for about a factor of 3, the predicted  $Q_e$  can change for more than an order of magnitude. We also note that although  $q$ ,  $\hat{s}$ , and  $\nu_{ei}$  also change in the high- $k$  measurement region as shown in Table II, their

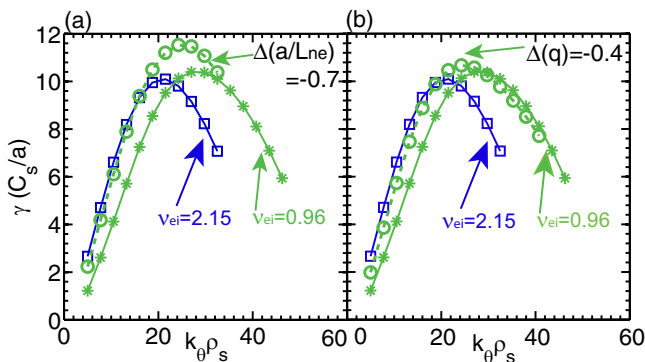


FIG. 19. (a) Linear growth rate spectra of the high collisionality shot (open square), the low collisionality shot (asterisks), and a scan in density gradient (open circle) with  $a/L_{n_e}$  reduced by 0.7 based on the parameters of the low collisionality shot to match that of the high collisionality shot; (b) The same as (a) except that the scan is in  $q$  with  $q$  reduced by 0.4.

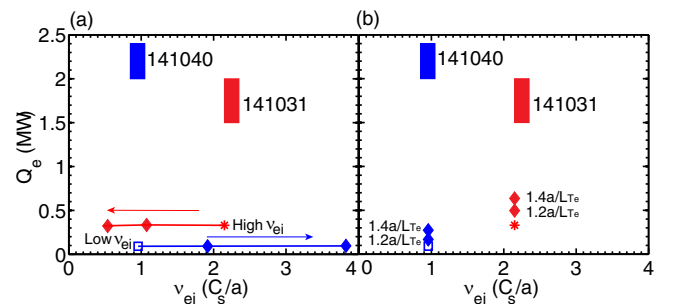


FIG. 20. (a) Experimental electron heat flux from TRANSP analysis (solid rectangles) and calculated  $Q_e$  from nonlinear GYRO simulations (asterisk for shot 141031 and open square for shot 141040) for the low and high collisionality shots using local Miller equilibrium as used for linear stability analysis shown in Fig. 18. Parametric scans (filled diamonds) in  $\nu_{ei}$  based on high collisionality shot and low collisionality parameters are also shown; (b) the same as (a), except that parametric scans are in  $a/L_{T_e}$ .

TABLE II. The ranges of some equilibrium quantities in the high- $k$  measurement region for shot 141040 from  $R = 133.5$  to  $137.5$  cm and for shot 141031 from  $R = 133$  to  $137$  cm. Parameters with large variation are highlighted in bold type.

shot	$r/a$	$q$	$\hat{s}$	$a/L_{ne}$	$\nu_{ei} (C_s/a)$	$\gamma_{E \times B} (C_s/a)$
141040	0.62 – 0.71	1.8 – 2.1	<b>0.8 – 1.9</b>	<b>0.7 – 2.7</b>	0.7 – 1.3	<b>0.2 – 0.5</b>
141031	0.57 – 0.65	1.5 – 1.7	0.9 – 1.3	<b>0.6 – 2.2</b>	1.9 – 2.8	<b>0.1 – 0.3</b>

profile variations do not correlate with the variations of the predicted  $Q_e$  profile as the density gradient in both shots. Although we believe that these parameters do affect the value of predicted  $Q_e$ , the density gradient remains the dominant parameter in determining the predicted  $Q_e$ . On the other hand,  $\gamma_{E \times B}$  profiles are also anti-correlated with the predicted  $Q_e$  profiles. However, our nonlinear simulations (not shown) indicate that a factor of 3 increase in  $\gamma_{E \times B}$  only leads to about a factor of 2 decrease in predicted  $Q_e$ , unable to account for the more-than-an-order-of-magnitude change of the predicted  $Q_e$  found in the high- $k$  measurement region. This observation further supports the results in Sec. III that ETG modes can be significantly stabilized by density gradient both linearly and nonlinearly.

## V. DISCUSSION AND SUMMARY

In this paper, we have presented experimental and numerical studies of parametric dependence of electron-scale turbulence on density gradient and electron collisionality. In the study of the density gradient dependence, we have demonstrated the density gradient stabilization of electron-scale turbulence by showing significant reduction in density fluctuation spectral power following a large core density gradient increase induced by an ELM event. We have also shown that the observed density gradient increase can lead to the stabilization of ETG instability by coupling with linear gyrokinetic stability analysis, which supports ETG instability as the source of the turbulence we observe before the ELM event. TEM, on the other hand, is ruled out by this observation, since our linear ion-scale GS2 calculations shows that TEM should be destabilized by the large density gradient after the ELM event (Fig. 8). We also note that although other relevant equilibrium quantities have much smaller change than the density gradient (see Fig. 6), they could still contribute to

the observed changes in both turbulence and transport, and further studies on these parameters will be performed in the future work. We also observed that density gradient strongly stabilizes smaller wavenumber modes,  $k_{\perp} \rho_s < 10$ , but may have little effects on higher wavenumber modes,  $k_{\perp} \rho_s \gtrsim 15$ , although a definite answer is out of the reach of the present data. We also note that even after being significantly reduced, the spectral power of the smaller wavenumber modes,  $k_{\perp} \rho_s < 10$ , are still finite, which may come from the small unstable region shown in Fig. 9(c), from turbulence spreading from unstable region to stable region<sup>47</sup> or from unstable TEM after the ELM event. Nonlinear global and/or multi-scale gyro-kinetic simulations will be needed to address this observation. A reduction in electron thermal diffusivity is also found to be correlated with the significant reduction of spectral power of the longer wavelength modes,  $k_{\perp} \rho_s \lesssim 10$ , suggesting the importance of these modes in driving anomalous plasma thermal diffusion. Nonlinear gyrokinetic simulations are able to reproduce the  $Q_e$  dependence on density gradient observed in the experiment. With a reasonable increase of ETG, the predicted  $Q_e$  is able to match the experimental  $Q_e$  before the ELM, but not after the ELM. It is found that after the ELM, the unstable TEM (Fig. 8) has growth rates large than the  $E \times B$  shearing rate, and preliminary ion-scale nonlinear simulations predict substantial transport. The reported strong stabilization effect of density gradient on ETG turbulence leads to the hope that density gradient may be able to used as tool to control micro-turbulence, i.e., a large enough density gradient to reduce ETG turbulence (actually ITG as well), but not large enough to enhance TEM in a significant way.

We also presented experimental and numerical studies of parametric dependence of electron-scale turbulence on electron collisionality, motivated by the observed strong confinement scaling with electron collisionality observed in NSTX (Ref. 11). As we have shown in Sec. IV, a complex picture of electron-scale turbulence has emerged from this collisionality scan. On the experimental side, we have successfully achieved varying local electron collisionality by a factor of about 2.5 with local  $\rho_e$ , local  $\beta_e$  and  $q_{95}$  kept approximately constant and with a confinement scaling consistent with that reported in Ref. 11. We would like to point out that despite of this consistency with the previously reported confinement scaling, the plasmas featured the present study are of lower local  $\beta_e$  (about 2%) and lower  $Z_{eff}$  (about 1.2) than the plasmas used in Ref. 11 ( $\beta_e \approx 8\%$  and  $Z_{eff} \approx 3$ ), and furthermore, ETG and ITG modes are found to be the most unstable modes (see Figs. 18 and 23), which is very different from the plasmas in Ref. 11, where microtearing mode is found to be the most unstable mode and ETG mode is found to be stable.<sup>37</sup> As shown in Table I, the change in the electron-ion collision frequency is much larger than the changes in the other equilibrium quantities in the scan, which seems to satisfy our goal of carrying out a dimensionless scan in electron collisionality. However, we point out that smaller changes in other parameters could still contribute to the observed change in turbulence (for example, see Fig. 19). The measured electron-scale turbulence spectral power appears to increase as collisionality is

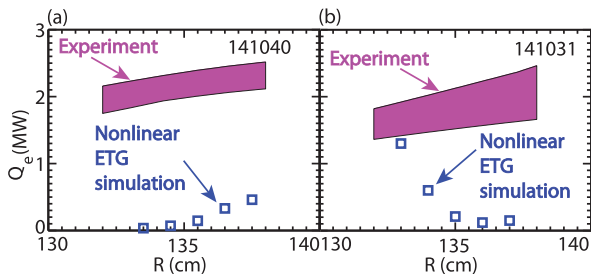


FIG. 21. (a)  $Q_e$  profile predicted by multiple local nonlinear ETG simulations (open square) and experimental  $Q_e$  profile (filled blocks) from power balance analysis using TRANSP for the low collisionality shot 141040; (b) the same as (a), but for the high collisionality shot 141031. The vertical width of filled blocks denotes the experimental uncertainty.

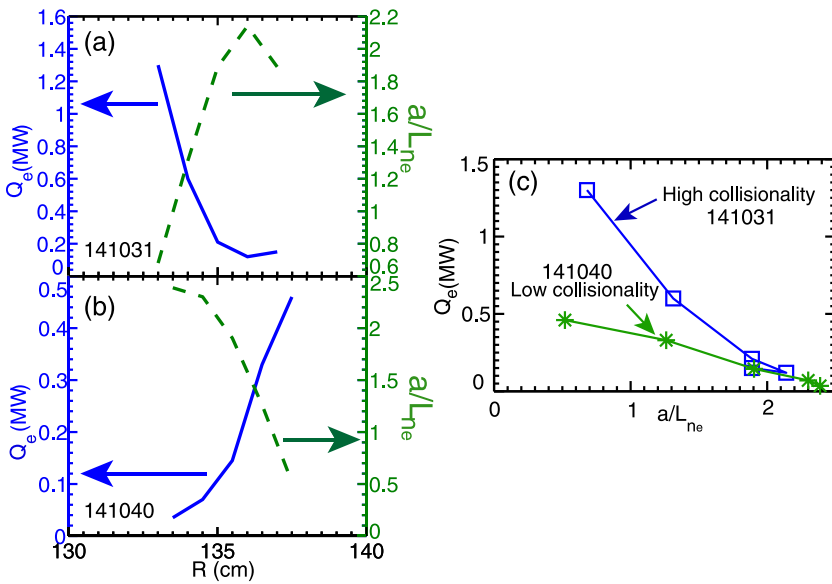


FIG. 22. (a) Predicted  $Q_e$  (blue solid line) and measured density gradient (green dashed line),  $a/L_{ne}$ , as a function of  $R$  in the high- $k$  measurement region for the low collisionality shot 141031; (b) the same as (a) except for the high collisionality shot 141040; (c) predicted  $Q_e$  as a function of density gradient for shot 141040 (green asterisk) and shot 141031 (open square).

decreased if we take into account the  $E \times B$  shear stabilization of lower wavenumber fluctuations as shown in Fig. 17. This observation seems to be inconsistent with the observed confinement dependence on electron collisionality where the normalized confinement time increases as electron collisionality decreases. Although the understanding of this discrepancy is still incomplete, as we will point out later, global multi-scale simulations and a synthetic diagnostic are necessary to explain this experimental observation.

On the theoretical side, local linear and nonlinear ETG gyrokinetic simulations have been carried out with the aim to elucidate experimental observations. Simulations with electron collisionality varied independently show that there is almost no dependence on electron collisionality in either the linear growth rate or nonlinearly generated electron heat flux. On the other hand, linear and nonlinear simulations using experimental profiles of the low and high collisionality shots clearly show a large difference in both the linear growth rate and nonlinearly generated electron heat flux; and with our still limited number of simulations (both linear and nonlinear), the difference appears to be dominated by density gradient variations, which is consistent with our observation presented in Sec. III. The large profile variation in the pre-

dicted  $Q_e$  within a 4 cm radial region, evident in Fig. 22, clearly shows that in these cases, ETG turbulence alone is not able to explain the observed electron thermal transport, and other mechanisms are needed. We note that the large profile variations in equilibrium quantities actually may make the contribution from ion-scale turbulence possible, and this can be seen in Fig. 23, which plots the radial profiles of  $E \times B$  shearing rate and the maximum ITG growth rate in the high- $k$  measurement region for shot 141040. Note that just within this 4 cm radial region (about  $6 \rho_i$ ), the  $E \times B$  shearing rate changes from more than 2 times larger than the maximum ITG growth rate, with which suppression of ITG turbulence is expected, to less than half of the maximum ITG growth rate, due to which ITG turbulence could survive. Given the large eddy size ( $\sim 6 \rho_i$ ) of ITG turbulence,<sup>48</sup> ITG turbulence growing at  $R = 137.5$  cm could affect the transport at  $R = 133.5$  cm. Thus, global ion-scale simulations, which take into account profile variations may well be needed for further understanding of electron thermal transport in these cases. In addition, since the turbulence measurement made by the high- $k$  scattering system averages over a region where large variation in fluctuation power could exist (as we have shown in Fig. 21), a synthetic diagnostic is required to simulate what the high- $k$  scattering system measures using density fluctuations from an appropriate global simulation. Note that when both ion-scale and electron-scale instabilities contribute to electron thermal transport, very likely for the cases we are considering there, multi-scale simulations would be needed to address the electron-scale fluctuations (which would be measured by the high- $k$  scattering system) nonlinearly driven by ion-scale turbulence. We note that global multi-scale simulations are very challenging, if not impossible, for the existing computational capabilities. Finally, we would like to point out that from what we have observed above, it is unlikely that ETG, ITG, TEM, or microtearing modes alone would be able to explain the same confinement scaling on electron collisionality observed in different plasma regimes, and most likely, it is the interplay between these modes (i.e., multi-scale) and also global effect (i.e., profile variation),

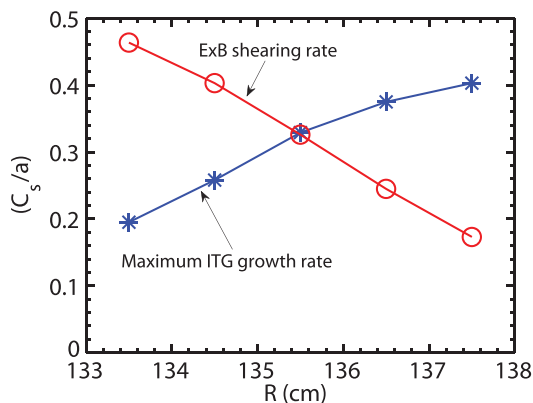


FIG. 23. The radial profiles of  $E \times B$  shearing rate and maximum ITG growth rate in the high- $k$  measurement region for shot 141040.

which are responsible for the observed confinement scaling. These issues will be addressed in future work.

## ACKNOWLEDGMENTS

The author would like to thank NSTX Team for the excellent technical support for this work. This work was supported by the U.S. Department of Energy under Contracts Nos. DE-AC02-09CH11466, DE-FG03-95ER54295, and DE-FG03-99ER54518.

- <sup>1</sup>W. Tang, *Nucl. Fusion* **18**, 1089 (1978).
- <sup>2</sup>B. Coppi and F. Pegoraro, *Nucl. Fusion* **17**, 969 (1977).
- <sup>3</sup>B. Kadomtsev and O. Pogutse, *Nucl. Fusion* **11**, 67 (1971).
- <sup>4</sup>R. D. Hazeltine and H. R. Strauss, *Phys. Rev. Lett.* **37**, 102 (1976).
- <sup>5</sup>J. F. Drake *et al.*, *Phys. Rev. Lett.* **44**, 994 (1980).
- <sup>6</sup>W. Guttenfelder *et al.*, *Phys. Plasmas* **19**, 022506 (2012).
- <sup>7</sup>Y. C. Lee *et al.*, *Phys. Fluids* **30**, 1331 (1987).
- <sup>8</sup>W. Dorland *et al.*, *Phys. Rev. Lett.* **85**, 5579 (2000).
- <sup>9</sup>D. R. Smith *et al.*, *Phys. Rev. Lett.* **102**, 225005 (2009).
- <sup>10</sup>M. Ono *et al.*, *Nucl. Fusion* **40**, 557 (2000).
- <sup>11</sup>S. M. Kaye *et al.*, *Nucl. Fusion* **47**, 499 (2007).
- <sup>12</sup>W. Horton *et al.*, *Nucl. Fusion* **45**, 976 (2005).
- <sup>13</sup>D. R. Smith *et al.*, *Rev. Sci. Instrum.* **79**, 123501 (2008).
- <sup>14</sup>E. Mazzucato *et al.*, *Phys. Rev. Lett.* **101**, 075001 (2008).
- <sup>15</sup>H. Y. Yuh *et al.*, *Phys. Rev. Lett.* **106**, 055003 (2011).
- <sup>16</sup>H. Y. Yuh *et al.*, *Phys. Plasmas* **16**, 056120 (2009).
- <sup>17</sup>Y. Ren *et al.*, *Phys. Rev. Lett.* **106**, 165005 (2011).
- <sup>18</sup>J. L. Peterson *et al.*, *Phys. Plasmas* **19**, 056120 (2012).
- <sup>19</sup>J. Candy and R. E. Waltz, *Phys. Rev. Lett.* **91**, 045001 (2003).
- <sup>20</sup>W. Guttenfelder and J. Candy, *Phys. Plasmas* **18**, 022506 (2011).
- <sup>21</sup>M. Kotschenreuther *et al.*, *Comput. Phys. Commun.* **88**, 128 (1995).
- <sup>22</sup>E. Mazzucato, *Phys. Plasmas* **10**, 753 (2003).
- <sup>23</sup>M. Romanelli *et al.*, *Phys. Plasmas* **11**, 3845 (2004).
- <sup>24</sup>F. Jenko *et al.*, *Phys. Plasmas* **8**, 4096 (2001).
- <sup>25</sup>M. Greenwald *et al.*, *Phys. Rev. Lett.* **53**, 352 (1984).
- <sup>26</sup>B. Balet *et al.*, *Nucl. Fusion* **30**, 2029 (1990).
- <sup>27</sup>P. Maget *et al.*, *Nucl. Fusion* **39**, 949 (1999).
- <sup>28</sup>F. Romanelli and S. Briguglio, *Phys. Fluids B* **2**, 754 (1990).
- <sup>29</sup>H. Zohm, *Plasma Phys. Controlled Fusion* **38**, 105 (1996).
- <sup>30</sup>B. P. LeBlanc *et al.*, *Rev. Sci. Instrum.* **74**, 1659 (2003).
- <sup>31</sup>R. E. Bell, *Rev. Sci. Instrum.* **77**, 10E902(2006).
- <sup>32</sup>J. E. Menard *et al.*, *Phys. Rev. Lett.* **97**, 095002 (2006).
- <sup>33</sup>F. M. Levinton *et al.*, *Phys. Plasmas* **14**, 056119 (2007).
- <sup>34</sup>T. S. Hahm and K. H. Burrell, *Phys. Plasmas* **2**, 1648 (1995).
- <sup>35</sup>S. M. Kaye *et al.*, *Phys. Rev. Lett.* **98**, 175002 (2007).
- <sup>36</sup>R. J. Hawryluk, *Physics of Plasma Close to Thermonuclear Conditions* (Pergamon, New York, 1981).
- <sup>37</sup>W. Guttenfelder *et al.*, *Phys. Rev. Lett.* **106**, 155004 (2011).
- <sup>38</sup>R. L. Miller *et al.*, *Phys. Plasmas* **5**, 973 (1998).
- <sup>39</sup>R. E. Waltz and R. L. Miller, *Phys. Plasmas* **6**, 4265 (1999).
- <sup>40</sup>J. Menard *et al.*, in *2011 IEEE/NPSS 24th Symposium on Fusion Engineering (SOFE)* (IEEE, 2011), pp. 1–8.
- <sup>41</sup>J. E. Menard *et al.*, *Nucl. Fusion* **51**, 103014 (2011).
- <sup>42</sup>W. Guttenfelder *et al.*, *Phys. Plasmas* **19**, 056119 (2012).
- <sup>43</sup>E.-j. Kim *et al.*, *Phys. Rev. Lett.* **91**, 075003 (2003).
- <sup>44</sup>S. E. Parker *et al.*, *AIP Conf. Proc.* **871**, 193 (2006).
- <sup>45</sup>K. C. Lee *et al.*, *Rev. Sci. Instrum.* **75**, 3433 (2004).
- <sup>46</sup>J. E. Kinsey *et al.*, *Phys. Plasmas* **14**, 102306 (2007).
- <sup>47</sup>Z. Lin and T. S. Hahm, *Phys. Plasmas* **11**, 1099 (2004).
- <sup>48</sup>T. L. Rhodes *et al.*, *Phys. Plasmas* **9**, 2141 (2002).